Boundary-Layer Meteorol (2012) 142:265–287
DOI 10.1007/s10546-011-9667-4

ARTICLE

Wind-Direction Effects on Urban-Type Flows

Jean Claus · O. Coceal · T. Glyn Thomas · S. Branford · S. E. Belcher · Ian P. Castro

Received: 28 June 2011 / Accepted: 19 October 2011 / Published online: 8 November 2011

Abstract Practically all extant work on flows over obstacle arrays, whether laboratory experiments or numerical modelling, is for cases where the oncoming wind is normal to salient faces of the obstacles. In the field, however, this is rarely the case. Here, simulations of flows at various directions over arrays of cubes representing typical urban canopy regions are presented and discussed. The computations are of both direct numerical simulation and large-eddy simulation type. Attention is concentrated on the differences in the mean flow within the canopy region arising from the different wind directions and the consequent effects on global properties such as the total surface drag, which can change very significantly—by up to a factor of three in some circumstances. It is shown that for a given Reynolds number the typical viscous forces are generally a rather larger fraction of the pressure forces (principally the drag) for non-normal than for normal wind directions and that, dependent on the surface morphology, the average flow direction deep within the canopy can be largely independent of the oncoming wind direction. Even for regular arrays of regular obstacles, a wind direction not normal to the obstacle faces can in general generate a lateral lift force (in the direction normal to the oncoming flow). The results demonstrate this and it is shown how computations in a finite domain with the oncoming flow generated by an appropriate forcing term (e.g. a pressure gradient) then lead inevitably to an oncoming wind direction aloft that is not aligned with the forcing term vector.

Keywords Surface forces · Urban canopy · Wind direction

J. Claus · T. G. Thomas · I. P. Castro (✉)
School of Engineering Sciences, University of Southampton, Southampton, UK
e-mail: i.castro@soton.ac.uk

O. Coceal · S. Branford · S. E. Belcher
Department of Meteorology, University of Reading, Reading, UK

1 Introduction

There is an increasingly large literature on flow and dispersion within urban environments. Not only have numerous field programmes been reported (e.g. Rotach 1993; Davidson et al. 1995; Roth 2000; Hanna et al. 2002; Dobre et al. 2005), but many authors have also addressed the issue by undertaking wind-tunnel experiments on boundary-layer flow over modelled sites (e.g. Perry et al. 2004; Kastner-Kline and Rotach 2005), rough surfaces comprising generic arrays of obstacles (e.g. Cheng and Castro 2002; Barlow and Belcher 2002) or by corresponding numerical computations (e.g. Coceal et al. 2006; Hanna et al. 2006; Xie and Castro 2006). To avoid having to compute the entire flow field within the canopy region—i.e. below the height of the tallest buildings—there have also been a number of simpler modelling approaches (e.g. Yamartino and Wiegand 1986; Coceal and Belcher 2004). In these studies, and practically all others in the literature, whether in the laboratory, through full numerical simulation or via simple analytical approaches, it is almost always the case that the surface morphology consisted of regular arrays of rectangular blocks aligned so that the oncoming wind is normal to block faces. In the field, however, the prevailing wind direction is only rarely in such alignment with the surface morphology. For example, the Marylebone Road area of London in the recent comprehensive field studies under the DAPPLE programme (Dobre et al. 2005) has around 100 mostly rectangular buildings in an essentially rectangular array surrounding streets in orthogonal directions. But the prevailing wind is typically aligned at around 51° to one of these directions.

It seems very likely that the surface drag generated for prevailing wind directions aligned at significant angles to building faces (as in the DAPPLE case) would be rather different to what it would be for a wind aligned with one or other of the street directions. Not only must the flow within the roughness canopy depend on the prevailing wind direction but, correspondingly, one would anticipate different values of roughness length (z_o) in the usual logarithmic law expression for the mean velocity profile in the inertial layer and, presumably, different values of the zero-plane displacement (d). Furthermore, the thickness of the roughness sublayer (that region of the flow above the canopy in which there are significant spatial inhomogeneities in horizontal planes) might also depend on wind direction and, given the different canopy flow, the mechanisms governing pollutant dispersion might also be significantly different.

The work of Bezpalcova (2006) is one of (as far as we are aware) only two wind-tunnel studies in the literature on the effect of different wind directions on flow and dispersion in urban-like arrays. She modelled in a wind tunnel the Mock Urban Setting Test (MUST) scaled field experiment conducted in the Utah desert (Biltoft 2001). The obstacles in the field experiment were shipping containers—with length 12.2 m, width 2.42 m and height 2.54 m and thus elongated in one direction—placed in an approximately rectangularly aligned layout. For this particular geometry, Bezpalcova came to the conclusion that the flow within the canopy was guided by the containers. For an oblique approach flow direction (for which field data were also obtained, Yee and Biltoft 2004), the velocity vectors below the building tops would quickly adjust so that they were oriented parallel with the streets along the length of the containers. It is unclear whether this is a general feature or whether it is linked to the particular building shape and layout in question. Hagishima et al. (2009) conducted a wind-tunnel study for more generic rectangular block arrays. They found that for square arrays a wind direction of 45° yielded block drag coefficients that were significantly higher than for the in-line wind direction, particularly for smaller plan area densities.

There have been a (very) few field experiments that include some data on wind-direction effects, notably those by Kanda et al. (2007) and Takimoto et al. (2011), who used arrays of large rectangular blocks and found some evidence of wind-direction effects. In particular, they found that wind directions at 45° yielded significantly larger roughness lengths, implying larger surface drag, than for flows at 0° or 90°, although individual datasets were naturally very scattered, as is typical for field experiments. The results presented herein provide some confirmation of this finding.

Kim and Baik (2004) is one of only two published articles (as far as we are aware) to report a numerical study of the effects of wind direction on the flow within urban-like arrays. They used an RNG $k - \varepsilon$ model, with a configuration of 16 buildings in an aligned layout and with area coverage of 25%. Several wind directions were simulated, from 0° to 45° every 5°. The authors noted three different general flow patterns in the street canyons. For the perpendicular wind direction ($\phi = 0°$), the flow was found to be symmetric about the centre of the canyon. A symmetric so-called portal vortex was observed behind the upwind building with its ends near the lower edges of the downwind building. For wind directions $5° \leq \phi \leq 20°$ the portal vortex was slightly tilted and asymmetric, with one footprint located near the street centre and the other near one edge of the upwind building (see their Fig. 4). For $25° \leq \phi \leq 45°$, the footprints of the portal vortex were located behind the end and side walls of the upwind building. These results were new and interesting, but there are serious questions about whether Reynolds-averaged Navier Stokes (RANS) methods are suitable for this kind of study (see Xie and Castro 2006, for example) and large-eddy simulation (LES) or direct numerical simulation (DNS) would most certainly be preferable. The other numerical study is that of Dejoan et al. (2010), who also considered the MUST field experiment, showing that LES predicted more significant wind-direction effects than did RANS. Overall, apart from the studies mentioned above, there has been remarkably little attention paid to the possible effects of wind direction on flows over urban-type roughness and it is this issue that we address in this paper. None of the above-mentioned work mentioned the possibility that the oncoming flow might produce transverse lift forces, although Dejoan et al. (2010) did note wind turning with height in some cases that, as argued in Sect. 2, is a natural consequence of such a force.

Both DNS and LES have been employed in the present work. It has already been shown that, at least for Reynolds numbers similar to those achieved in typical wind-tunnel modelling, current computing power is sufficient to allow fully resolved DNS (Coceal et al. 2006). It is also feasible to use LES on coarser grids or at much higher Reynolds numbers because, in many of these flows, the surface drag is dominated by pressure forces and nearly all of the turbulence energy both within and above the canopy is at scales similar to those of the roughness elements; viscous effects are thus usually insignificant and the subgrid and wall-region issues that bedevil the use of LES over smooth surfaces are much less significant (see Xie and Castro 2006, for a fuller discussion). However, these conclusions were reached on the basis of a wind flow normal to the faces of the obstacles in regular arrays having a 25% plan area ratio (λ_p in the usual terminology) and it turns out that for certain wind directions and morphologies, Reynolds number independence is less certain, as will be demonstrated. In all the present cases the surface morphology comprised regular arrays of cubes, but two different patterns have been considered: a square array (using DNS) and a staggered array (using LES), both with an area coverage of 25%. These are thus the same as in our earlier work and they provide perhaps the simplest generic urban-type geometries. Wind-direction effects for more random building array arrangements (e.g. as in the arrays of random height obstacles considered by Xie et al. (2008)) provide the next step in complication, although it

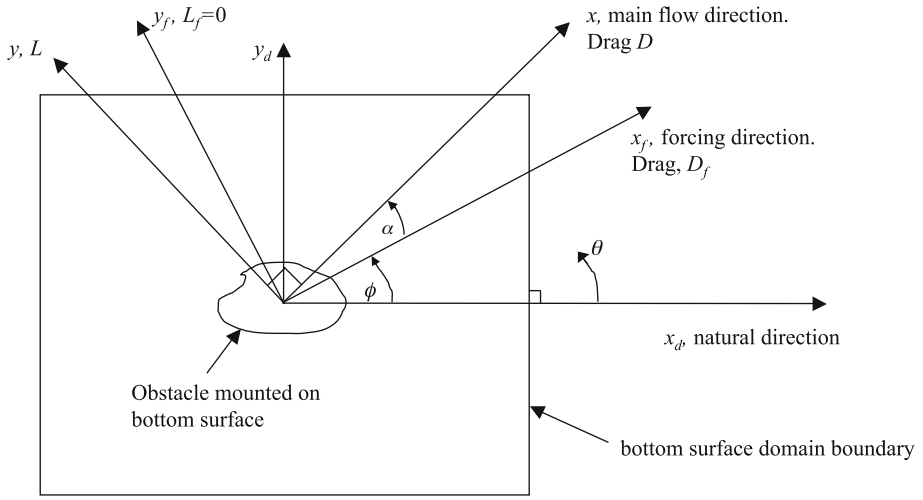

Fig. 1 Domain surrounding arbitrary lifting body, showing forcing direction and resulting lift and drag forces. x is the main flow direction (well above the body)

seems likely that the general conclusions discussed here may well be applicable qualitatively to more complex circumstances.

It should also be emphasized that our computations allow a much more complete assessment of the flows than is presented here, where attention is concentrated only on the mean flow and, furthermore, mostly on the mean flow spatially-averaged in horizontal planes. We do not, for example, consider here details of the turbulence field, either its local characteristics within the canopy or its spatially-averaged nature. This is not to say that such matters are not important (they will be the subject of future work), but including them here would undoubtedly detract from the major issues surrounding the effects of wind direction on the average mean flow and its characteristics, including those of the mean pressure field on the obstacles.

The paper is organized as follows: Sect. 3 presents a summary of the methodology; this is intentionally brief as fuller details are given in our earlier work. Section 4 presents the major results and discussion, whilst Sect. 5 contains further discussion and summarizes the major conclusions. First, however, it is important to consider the problem in general terms. This is done in the following section, which sets the scene for the simulations and provides a basis for the later presentation and analysis of results.

2 General Considerations

We discuss here the fundamental character and effects of the forces generated by a flow over a general rough surface, whether modelled in a wind tunnel or computed numerically. Consider an arbitrary object, which in the present context would represent the entire bottom (rough) surface of a boundary layer, located within a rectangular domain as shown in Fig. 1. (It could equally well be a finite aspect-ratio wing mounted vertically on the bottom surface of the domain). The object is supposed sufficiently general that it may generate drag D and lift L forces along and normal to, respectively, the oncoming flow direction (at the top of the domain), which for the moment we designate as x, in a direction that may be offset from the

forcing direction by some angle α (which can in practice be of either sign, or zero). Note that we use lift here to mean the force in the horizontal plane normal to the usual drag force (i.e. *not* the force in the vertical direction, which might also of course be non-zero but does not contribute to the total surface stress). To avoid confusion, however, we henceforth usually refer to this lift as the lateral force. Both drag and lateral forces arise solely from pressure or viscous forces acting on the obstacle surfaces, or a combination of the two. In principle, a non-zero lateral force will usually occur if the flow field around the object is asymmetrical in a direction normal to the oncoming mean flow, which can arise from any type of geometrical asymmetry in the object, even if the object (as in the present work) is composed of arbitrary rectangular obstacles whose faces are normal to the oncoming flow. In a wind-tunnel experiment, the lateral domain boundaries are most naturally the tunnel side walls and the forcing and flow directions are coincident and parallel to these so that, in the notation of Fig. 1, $\alpha = \phi = 0$ and $x \equiv x_\mathrm{d} \equiv x_\mathrm{f}$. Any (total) lateral force generated by the flow over the obstacle must appear as an (equal and opposite) difference in static pressure forces acting on the two lateral boundaries and in the present context of a rough surface boundary layer the flow well above the boundary layer must be in the x ($= x_\mathrm{d}, \alpha = 0$) direction. Within the boundary layer, the flow will turn laterally if there is a non-zero lateral force, but there are then implications about side-wall influences, for near them there can be no net lateral mass flux.

In a numerical simulation, in contrast, the forcing may be applied at an arbitrary direction (ϕ) to the domain boundaries and it is common to apply periodic (cyclic) conditions on both the axial and lateral boundaries, generating a fully-developed channel flow. Note that, for an urban canopy on the bottom surface, provided the domain depth H is sufficiently large, this produces a flow within and just above the canopy region that is essentially the same as it would be in a regular developing boundary layer whose thickness δ is similar to H. (Incidentally, careful thought is required in applying the cyclic boundary conditions appropriately in the general case of $\phi \neq 0$.) Since there is neither a momentum flux change across the lateral boundaries nor a pressure difference between them, the obstacle's total force vector component in the direction normal to the forcing direction must be identically zero: hence $L_\mathrm{f} = 0$, see Fig. 1. It is an inevitable consequence that the resulting flow direction (x) 'seen' by the obstacle cannot be in the forcing direction unless the obstacle is such as to yield zero lift (lateral) force normal to the flow direction. Rather, there will in general be some non-zero α, such that $\tan\alpha = -L/D$. Note that it is best to restrict 'drag' and 'lift' to their usual meaning—the fundamental forces in the flow direction and normal to it, respectively. D_f and L_f should be thought of simply as forces obtained by suitable transformations of D and L, *not* as drag and lift. And we emphasize that by 'flow direction' we mean the direction of the mean flow at the top of the domain.

It is clear that supplying a particular forcing direction will only in special circumstances lead to a flow direction aligned with it. The situation is similar if a particular fixed inlet (and thus outlet) mass flux is specified rather than a fixed pressure gradient; this is just an alternative way of providing the forcing. So numerical codes will in the general case not allow *a priori* a precise specification of the flow direction over the rough surface. Provided the lateral force (L) is very small compared with the drag force, the resulting misalignment between the forcing direction and the resulting flow direction will of course also be small. It will be seen below that typically, for the urban-type surfaces considered here, $|\alpha| \lessapprox 4°$, which is small enough to be considered negligible in field situations. Recall that practically all the extant work on flow over arrays of obstacles has considered only what might be called the pathological cases in which the surface morphology is such as to ensure that $\alpha = 0$ (i.e. $L = 0$). We emphasize that there are of course much larger wind directional changes within

Table 1 Definitions for the various surface forces—see Fig. 1

Force	Definition
D	Total drag force acting in the main flow direction
D_{f}	Total drag force acting in the forcing direction
L	Total lateral ('lift') force acting normal to the main flow direction
L_{f}	Total lateral ('lift') force acting normal to the forcing direction
D_{pr}, D_{fpr}	Pressure components of the drag forces, D and D_{f}, respectively
L_{pr}, L_{fpr}	Pressure components of the 'lift' forces, L and L_{f}, respectively
D_{fr}, D_{ffr}	Frictional components of the drag forces, D and D_{f}, respectively
L_{fr}, L_{ffr}	Frictional components of the 'lift' forces, L and L_{f}, respectively

All forces refer in the present case to those acting on a unit element of the obstacle array (i.e. a $2h \times 2h$ area containing one cube of side h)

the urban canopy, because of effects like flow channelling along streets; this is discussed in detail later. These effects locally overwhelm the effect caused by the lateral force but they have a fundamentally different physical cause than that discussed above and (as will be seen) they do not propagate much above the canopy.

It is also worth pointing out here that if, in any particular computed case, there is a non-zero pressure force component to L_{f}, L_{fpr} say, then this must be balanced by an equal and opposite force, L_{ffr} say, arising from frictional effects at the surfaces, to ensure that $L_{\mathrm{f}} = 0$ (i.e. $L_{fpr} + L_{ffr} = L_{\mathrm{f}} = 0$). To help clarify thinking about the notation for the various component forces they are listed and defined again in Table 1.

Finally, a comment about the corresponding field situation is appropriate. In this case there are no constraining axial or lateral boundaries and forcing of the entire flow is actually applied by the geostrophic pressure gradient; Ekman turning of the wind is inevitable even over a notionally smooth surface. This is a complicating factor but for simplicity of thinking and for the present purposes the forcing direction might be considered as the upstream wind-vector direction at a height of, say, 200 m (well above the tops of the buildings). These buildings will in general collectively produce a (usually small) lift force normal to this, which implies a circulation, in the aerodynamic sense, around the entire array. There will thus be inevitable flow turning downwind quite independently of any Coriolis effects, but whether such turning becomes noticeable within the array will depend on the fetch. The major issues here, however, are the extent to which different wind-vector directions over the same array lead to different effective surface roughness, surface drag and canopy flow, and there is no reason why both wind-tunnel and numerical simulations should not address these issues in order to provide information relevant to full-scale field situations. Nonetheless, in the light of the above discussion it is important to note the effects of the specific lateral boundary conditions used for such simulations. It is also worth noting that laboratory scale simulations of real sites that may produce significant lift should be designed carefully as the effects of lateral boundary constraints are likely to be more significant.

3 Numerical Approaches

The DNS code was originally formulated by one of the present authors (TGT), as discussed in Yao et al. (2001) and briefly described in the context of rough surfaces by Coceal et al.

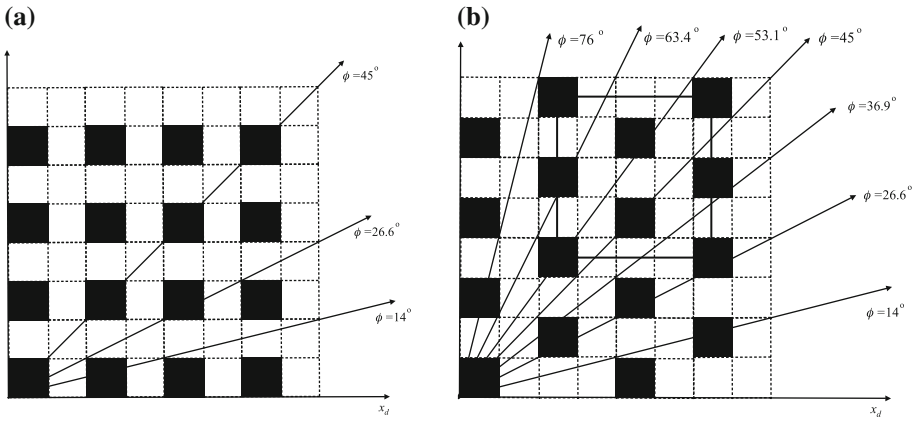

Fig. 2 Plan view of the domains. **a** Square array (for DNS); **b** staggered array (for LES). In **b** the actual domain contained only four *cubes*, like the square domain outlined by the *solid line*

(2006). It essentially solves a second-order (in space and time) central differenced version of the Navier–Stokes equations, using a pressure correction method, a multi-block mapping strategy and a multi-grid method for the pressure solution. In the present work the domain size was usually $8h \times 8h \times 4h$ and Fig. 2a shows a plan view of the bottom of the domain, identifying the sixteen cubes in a square array. This arrangement has symmetry axes at 45° to the streets as well as along them (i.e. at 0° and 90°), so computations with forcing directions (x_f, see Fig. 1) only in the range $0° \leq \phi \leq 45°$ were necessary; we chose $\phi = 0°$, 14°, 27° and 45°, as indicated in Fig. 2a. A uniform Cartesian mesh was used, with a mesh spacing equal in all directions and of size $h/32$, identical with that of the earlier DNS of Coceal et al. (2006). It was shown there that (for the present Reynolds number, see below) the grid size lay between 4η and 8η where η is the Kolmogorov length scale, which is more than sufficient to capture the major part of the dissipation spectrum; the computations are thus well resolved. Periodic boundary conditions were applied, with free slip conditions at the top of the domain, $z = 4h$. Note that Coceal et al. (2006) demonstrated that this domain height (H) led to flows within and just above the canopy region essentially the same as those found with higher domains (like $H = 6h$ or $H = 8h$), so $4h$ was chosen in order to minimize the necessary computational effort.

The flow was maintained by imposing a height-independent pressure gradient in the forcing direction, via an appropriate forcing term added to the equations for each cell in the fluid domain. As discussed in Sect. 2, this total applied force must be balanced by the total surface force acting in the opposite direction and thus is proportional to ρu_τ^2, where u_τ is the wall friction velocity defined as $\sqrt{\tau_w/\rho}$ with τ_w the total wall-stress component in the forcing direction (x_f). The Reynolds number ($u_\tau h/\nu$) was 500, so that the flows are well into the fully rough regime (but see later); Reynolds numbers based on the velocity at the top of the domain and the cube height were typically around 5,000. All simulations were run for an initial duration of $200T$, where $T = h/u_\tau$, the turnover time for the typical eddies shed by the cubes. Statistics were then averaged over a further $400T$ at least, to ensure convergence, with a timestep of $0.00025T$. These long averaging times are necessary because of the possible existence of longitudinal rolls above the canopy, which move around over long time scales and give rise to non-zero residual dispersive stresses if the averaging time is too short (see Coceal et al. 2006; Leonardi and Castro 2010, for discussion of this point). Each run was

performed using typically 240 processors on an IBM JS21 supercomputer at the University of Reading and required typically 240 h computing time.

For the LES, the commercial code STAR-CD4 (from CD-adapco) was used for computations of flow over a staggered, rather than square, array of cubes with the same plan area ratio (λ_p in the usual notation) as in the DNS—25%—as shown in Fig. 2b. Note that the forcing directions $\phi = 0°$ and $\phi = 90°$ correspond to the configurations that Coceal et al. (2006) termed 'staggered' and 'aligned' arrays, respectively. It has been shown previously (Xie and Castro 2006) that with second-order differencing in time and space and provided (Cartesian or polyhedral) meshes in the canopy region have cell sizes no larger than $h/16$, the LES approach, at least for the $\phi = 90°$ case, produces results that are close to both experiment and fully-resolved DNS, for the Reynolds numbers typically used (similar to those in wind-tunnel experiments and, as for the DNS described above, of order 10^4). A model similar to the classical Smagorinsky approach was used with $C_s = 0.1$ (Yoshizawa 1986), with the Lilley damping function applied in regions very close to all surfaces, but we emphasize that since in the canopy region the turbulence is dominated by large scales (unlike above smooth walls), the results are not likely to be very dependent on the details of the near-wall methodology (but see later). Forcing was applied in the same way as in the DNS. The effective forcing angles were $\phi = 0°$, 14°, 27°, 37°, 45°, 53°, 63° and 90°. The mesh had grid sizes of $h/32$ next to all horizontal surfaces, expanding to no more than $h/16$ within the canopy and $h/12$ above $z = 1.5h$. To reduce computational effort, the domain was smaller than that used in the DNS computations, containing only four cubes (see Fig. 2b). All simulations were run using a timestep of $0.0001T$ for an initial duration of $200T$, with statistical averaging performed over the subsequent $300T$. Runs were performed on the IRIDIS2 cluster supercomputer at Southampton University, using typically 16 or 32 processors. With this smaller number of processors, significantly longer times were required to obtain converged results than for the DNS cases.

Additional runs were made using larger domain sizes for both the square and the staggered arrays. Checks showed that, as far as the results presented herein are concerned, they were essentially independent of the domain's axial and lateral extent, as found in earlier work (Coceal et al. 2006; Xie and Castro 2006). On the other hand, changes in domain heights (from the $4H$ used here for both roughness types) naturally yielded different bulk velocities for a given wall stress, for example. But, again, checks showed that increasing the domain height did not change quantities like the spanwise lift to axial drag on the cubes, so details of the pressure and mean velocity fields within the canopy region are not believed to be strongly dependent on domain height.

It should be emphasized at this point that in the following sections all the data referring to the square roughness array were obtained using DNS, whereas all those for the staggered array were obtained using LES (as clarified in Fig. 2). The reason for using the two different approaches was largely circumstantial; the latter formed a major part of the work of Claus (2011), whereas the former was part of a quite separate and wider investigation of dispersion in urban canopies (Branford et al. 2011). It has been demonstrated previously that, provided the LES technique is used appropriately, it yields results close to those given by full DNS or by laboratory measurements (Xie and Castro 2006), at least for the typical flow Reynolds numbers used here. We comment further on this later, but note immediately that we believe the distinct physical differences in the flow over the two surfaces explored in the following sections are not related in any way to the different numerical approaches used.

4 Results

4.1 The Pressure Field

4.1.1 The Overall Force Balance

In view of the general discussion in Sect. 2 it is appropriate to start first with a consideration of the way that the forcing direction ϕ affects the drag and lift forces on the obstacles. To help clarify the two different cases, Fig. 3 provides a reminder of the notation. Figure 4 shows how the pressure difference across a cube in the forcing direction depends on the array type and ϕ. The data have been normalized so that if frictional forces were negligible the integral of each distribution would be exactly unity. In fact, the total pressure force, $D_{f_{pr}}$, differs from unity in every case, as can be deduced from the figures. These pressure forces are very close to those referred to coordinates aligned with the flow direction (because α never exceeds 4°) and integrated values of the latter—i.e. the total pressure drag D_{pr}—are given in Table 2, which is discussed in more detail in due course. For both roughness types it is clear from Fig. 4 that for directions not aligned with the cube faces there is a much less pronounced increase in sectional pressure force towards the top of the canopy. This means that, unlike the classically studied $\phi = 0°$ case, the earlier finding that the surface drag is dominated by the upper parts of the buildings is more generally *not* the case.

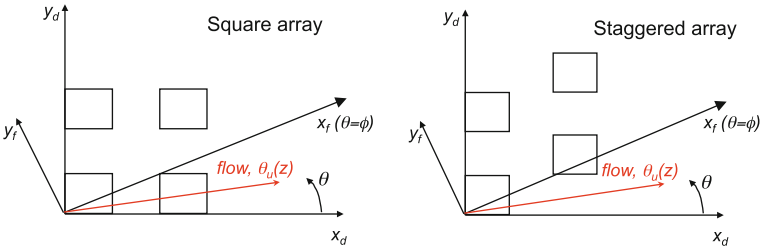

Fig. 3 Notation for the two array cases. $\theta_u(z)$ is defined as the spatially-averaged flow direction at height z. The particular case of a forcing direction of $\phi = 27°$ is shown

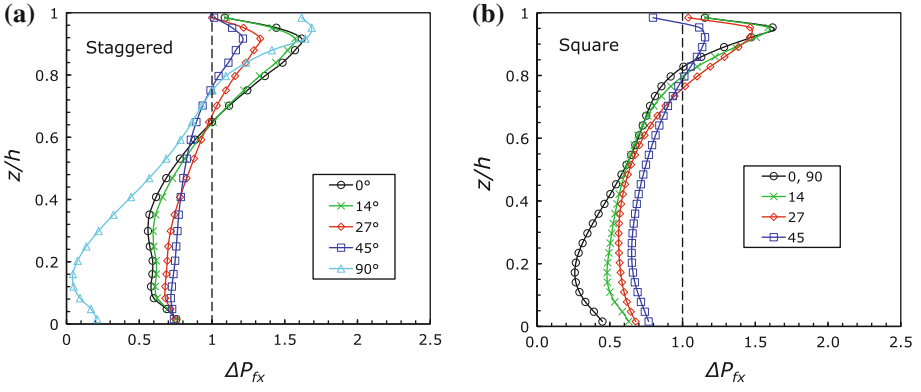

Fig. 4 Vertical variations of the laterally integrated front-to-back pressure differences, in the forcing direction for **a** staggered array, **b** square array. *Legends* indicate the forcing direction ϕ for each case

Table 2 Salient force values and angles for each case. The forces are referred to coordinates parallel and normal to the flow direction—i.e. at α to the forcing direction ϕ

Array type	ϕ	D_{pr}	L_{pr}	$\alpha_{f_{pr}}$	α	$\overline{U}/u_\tau$
Staggered	0	0.903	0.0	0.0	0.0	24.6
Staggered	14	0.913	−0.0185	−0.02	1.14	27.7
Staggered	27	0.905	0.0292	0.59	−1.26	26.3
Staggered	37	0.904	0.0648	1.24	−2.87	22.7
Staggered	45	0.873	0.0686	1.83	−2.66	25.0
Staggered	54	0.865	0.0374	2.1	−0.38	25.1
Staggered	63	0.838	−0.0470	−0.01	3.2	27.4
Staggered	76	0.752	−0.0366	−1.54	1.25	32.1
Staggered	90	0.672	0.0	0.0	0.0	34.9
Square	0	0.664	0.0	0.0	0.0	31.9
Square	14	0.755	0.0339	−1.00	−3.57	26.6
Square	27	0.802	−0.0121	−2.40	−1.54	24.9
Square	45	0.813	0.0	0.0	0.0	16.6

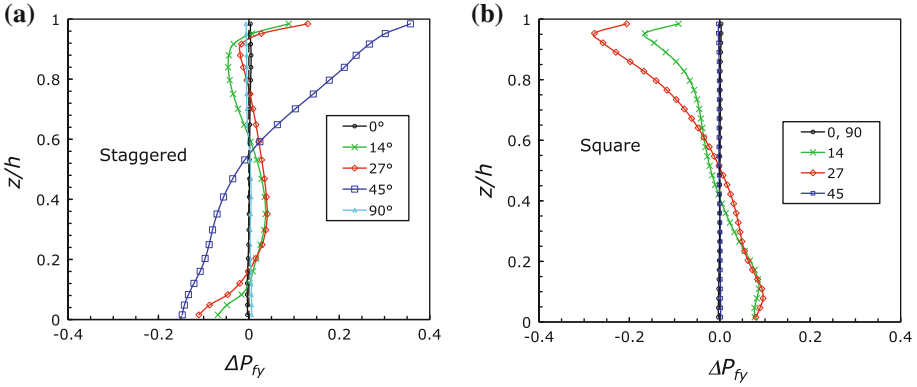

Fig. 5 Vertical variations of the laterally-integrated front-to-back pressure differences, normal to the forcing direction for **a** staggered array, **b** square array. *Legends* indicate the forcing direction ϕ for each case

Profiles of the corresponding pressure forces acting normal to the forcing direction are shown in Fig. 5. (For symmetrical cases, these sectional forces are indistinguishable from zero, as expected.) A major feature is that the forces over the top region of the cubes ($z/h > 0.92$) are of opposite sign in the two arrays, but immediately below that the forces have the same sign in the $\phi = 14°$ and 27° cases but are much larger for the square array. For the staggered array, the forces are generally of opposite sign for $\phi = 45°$ than for the other directions. Since $\theta = 45°$ is a symmetry axis in the square array, it is perhaps not surprising that the maximal sectional lifts occur for $\phi = 27°$, whereas for the staggered array they occur for $\phi = 45°$—roughly half way between two symmetry planes in each case. Note that only if these lateral pressure forces integrate to zero over the height of the cube would there be no frictional force contribution in the lateral direction. (Recall that, as explained in Sect. 2, the sum of the pressure and frictional forces in the direction normal to the forcing must be zero.) Table 2 includes the value of the lateral force, the 'lift' L_{pr}, arising from the pressure

distribution on the cube (in the direction normal to the flow direction), along with the values of $\alpha_{f_{pr}}$ and α for every case. The former is the angle between the total pressure force vector and the forcing direction and the latter is the effective flow angle (the angle between the flow direction at the top of the domain and the forcing direction); in terms of the notation in Fig. 3 $\alpha = \theta_u(H) - \phi$.

For both arrays, the integrated pressure force in the lateral direction, $L_{f_{pr}}$, never exceeds about 3% of the force in the forcing direction itself (although this can rise to nearly 7% when referred to flow coordinates, as Table 2 indicates). This implies that there are in some cases small lateral frictional forces, which implies that Reynolds number effects may not be entirely insignificant. Reynolds number effects are implied more obviously by the values of the (normalized) pressure force in the forcing direction. When the latter is aligned such that there are unobstructed 'streets' in the forcing direction, $D_{f_{pr}}$ (which is very close to D_{pr} because α is small) can be as low as 0.66; recall that the normalization is such that it would be unity in the absence of frictional effects. This implies much more significant Reynolds number effects than have generally been anticipated for roughness that fully blocks the oncoming flow (e.g. $\phi = 0$ for the staggered array, as in Coceal et al. 2006; Xie and Castro 2006). Such effects would only be properly captured by fully-resolved DNS or by LES approaches that embody much better wall conditions than usual.

The force results given in Table 2 are presented in Fig. 6a, where the (pressure) lift and drag are shown as a function of the forcing angle. Recall that the forces have been normalized so that if frictional forces were zero then D would be very close to unity (not exactly unity, since the flow angle is not exactly the same as the forcing direction, but the difference from unity would not be noticeable on the figure). So the difference between D and unity is a measure of the frictional effects. It is worth emphasizing a few points. Firstly, as noted above, it is clear that the frictional contribution has qualitatively different behaviour for the two array types. It is larger for forcing directions most nearly aligned to street directions, with the largest occurring for $\phi = 90°$. This is intuitively what one would expect; open streets running in the overall flow direction lead to the highest near-surface velocities (see later) and thus presumably the largest frictional surface stresses. Secondly, it is interesting that the arrangement of the cubes has little effect on the frictional contribution in this $\phi = 90°$

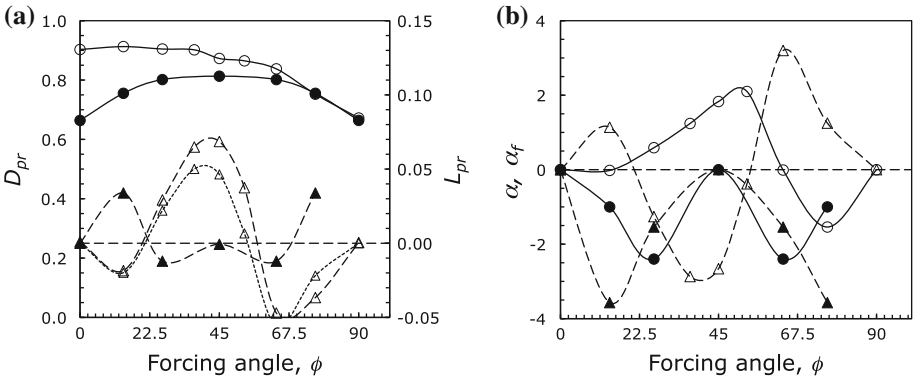

Fig. 6 Variations with forcing angle of **a** the pressure drag and lift forces (normalized by the total forcing). ○, drag; △, lift. The *dotted line* marked by open triangles is the lift that would occur in the absence of frictional effects (i.e. with $D_{fx} = 1$). **b** The flow and pressure force vector angles (in *degrees*), with respect to the forcing direction. ○, α_f; △, α. *Open* and *closed symbols* in both figures refer to staggered and square arrays, respectively

direction, suggesting that the largest frictional contribution is indeed within the open streets rather than between the cubes, where there are recirculating regions and generally much lower velocities irrespective of whether the cubes are just $1.0h$ apart in the wind direction (in the square array) or $3.0h$ apart (in the staggered array).

Thirdly, even in the absence of frictional forces, one expects non-zero lift forces if the flow angle is not aligned with the forcing direction. There seems little reason to suppose that frictional processes would have a large effect on these angles, so Fig. 6a includes the lift that would be expected in the absence of friction but assuming that the flow angle (α) remains the same. This lift force, $L_{pr} = L_{f_{pr}} \cos\alpha - D_{f_{pr}} \sin\alpha$, would then be simply $-1.0 \sin\alpha$ (for $D_{f_{pr}} = 1$ and $L_{f_{pr}} = 0$). The results, shown only for the staggered array, are very close to those computed using the actual $D_{f_{pr}}$ and $L_{f_{pr}}$, suggesting that the frictional contributions to the total lift force are very small compared to those for the total drag force.

It should be emphasized that the pressure lift force is anyway always small compared with the drag, but it is interesting that for the square array the lift usually acts in the opposite direction than it does for the staggered array. Figure 6b shows how the angle data vary with forcing direction (Table 2). Neither $|\alpha|$ nor $|\alpha_{f_{pr}}|$ ever exceeds four degrees, so the pressure force in the forcing direction is always very close to the true pressure drag-the pressure force in the flow direction (i.e. $D_{f_{pr}} \approx D_{pr}$ as noted earlier). The variations of the flow direction, α, measured with respect to the forcing direction and seen in Fig. 6b naturally mirror the corresponding lift variations seen in Fig. 6a; note too that the angle made by the total pressure force vector, $\alpha_{f_{pr}}$, is also generally of opposite sign for the two array types, except for forcing directions in excess of about 65°.

4.1.2 Canopy Surface Pressure Details

It is worth considering briefly the individual pressure fields over the cube surfaces that give rise to the global pressure forces discussed above. Figure 7 presents a selection of pressure contours for both staggered and square arrays. The forcing direction is indicated on each plot and the purpose of these figures is simply to compare qualitatively some features of the different cases. For $\phi = 0°$ (Figs. 7a,b) the side-wall pressure fields are very similar, but there are noticeable differences on the front and rear faces between the two array types. The high pressure values near the top-centre of the front face of the cube in the square array are not mitigated by rapid falls in pressure nearer the sides, as they are in the staggered array, which is why the peak front-to-back pressure difference in Fig. 4 is noticeably higher for the square array. For $\phi = 45°$, in contrast, the fields are very different. The expected symmetric pattern about $\theta = 45°$ for the square array (Fig. 7d) compared with the expected asymmetric pattern for the staggered array (Fig. 7c) about that or any other axis is clear. In the staggered case, higher and more concentrated peak pressures occur on face B than on face A, because the former faces a more open street arrangement than the latter. It is the asymmetry that leads to the non-zero variations in side-to-side pressure differences seen in Fig. 5a and the consequent non-zero total lift force (Table 2).

For the staggered array, although $\phi = 90°$ is a symmetry direction, note that the surface pressure field (Fig. 7g) differs somewhat from that at $\phi = 0°$ (Fig. 7a). The major difference is in the patterns on the 'front' face—i.e. the surface facing the main flow, face A for $\phi = 0°$ (Fig. 7a) but face B for $\phi = 90°$ (Fig. 7g). For the latter case the pressures are generally rather lower, because that face is much nearer the rear face of the upstream cube. This leads to the front-to-back pressure differences being closer to zero than they are for $\phi = 0°$, as seen in Fig. 4a. It is also worth pointing out that the pressure distributions at $\phi = 90°$ are very similar for the two arrays (compare Fig. 7g with Fig. 7b—noting that the latter is identical to the

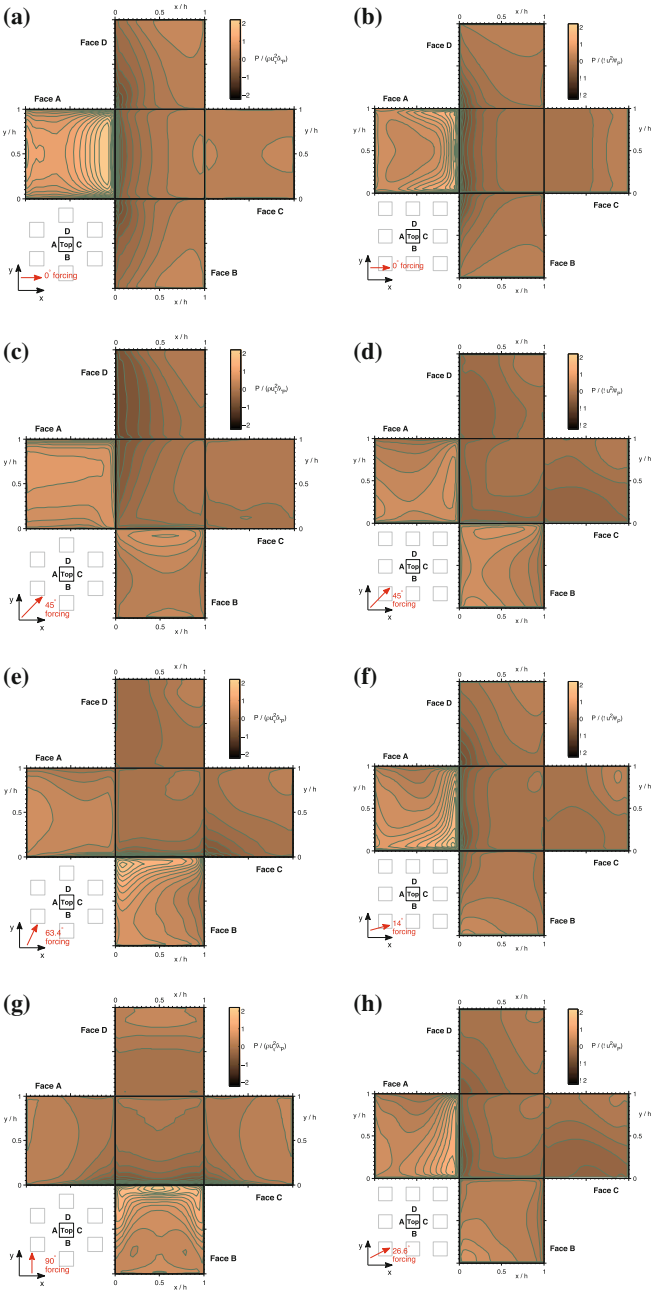

Fig. 7 Contours of surface pressure on the five faces of the cube. **a**,**c**,**e**,**g**—i.e. *left-hand side* staggered array; **b**,**d**,**f**,**h**—i.e. *right-hand side* square array. $\phi =$: **a**,**b** 0°; **c**,**d** 45°; **e** 63°; **f** 14°; **g** 90°; **h** 27°. The *contour scale* is identical in every case, with pressure coefficients normalized in the same way as the laterally-integrated values shown in Fig. 4

$\phi = 90°$ orientation because of symmetry). This is reflected in the similarity in the pressure drag contribution to total drag between the two cases, as shown in Fig. 6a and discussed earlier. Finally, the two intermediate orientations for the square array (Figs. 7f,h for $\phi = 14°$ and 27° respectively) are quite similar, which is why both front-to-back and side-to-side integrated pressure difference profiles (Figs. 4b, 5b) have the same character. The $\phi = 63°$ staggered array case (Fig. 7e) has a surface pressure field clearly intermediate between the $\phi = 45°$ and 90° cases, with the highest pressures now occurring, not surprisingly, on the face most closely normal to the forcing direction (face B).

4.2 Spatially-averaged Velocities

4.2.1 Global Details

Figure 8 shows the profiles of horizontally-averaged mean velocity (normalized by the friction velocity) for both array types at various forcing directions, ϕ. The velocity at each height was obtained by averaging first over time (see Sect. 2) and then horizontally over the entire computational domain. (Only a selection of forcing directions are shown for the staggered array case.) It is immediately obvious that the profiles are strongly dependent on ϕ. The velocities have been normalized by the friction velocity, u_τ, so the data imply that the total 'mass flux'—characterized by the bulk velocity defined as $U_b^+ = \frac{1}{H}\int_0^H U^+ \mathrm{d}z$—is very dependent on ϕ and, for a given ϕ, on the array type. This is a major result but it is not unexpected. It means that the drag of a given surface type depends on its orientation to the forcing. The result is emphasized by Fig. 9, which shows how U_b^+ varies with forcing direction. Note that whilst the plan area ratio, λ_p, is independent of ϕ, the frontal area ratio λ_f, which is a measure of the flow blockage provided by the cube array, is clearly not. λ_f is defined as the ratio of the solid area projected in the forcing direction to the plan surface area for any given repeating unit—$2h \times 2h$ for the present cases. The figure includes the variation of λ_f; it is independent of whether the array is square or staggered and rises to a maximum at $\phi = 45°$ of some 40% higher than at $\phi = 0°$ or 90°.

For the square array, there is a symmetric correspondence between the degree of flow blocking, measured by λ_f, and the mass flux that results from the applied forcing—higher blocking yields a lower flow rate, as might be expected. The extent of the reduction in flow

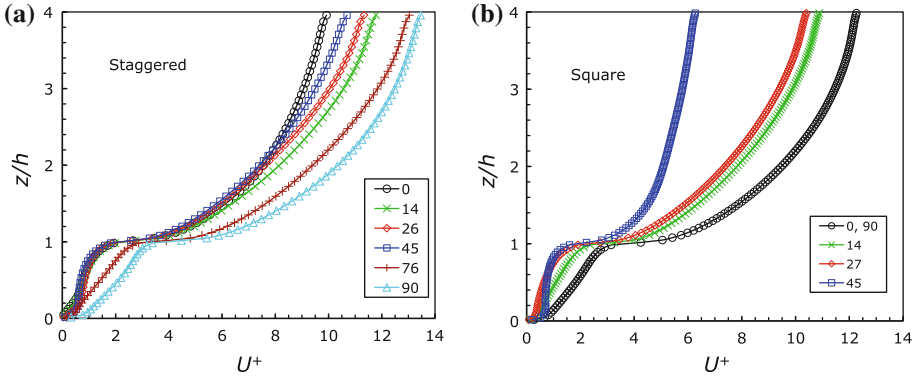

Fig. 8 Vertical variations of the spatially-averaged velocity in the flow direction for **a** the staggered and **b** the square array. *Legends* indicate the forcing direction ϕ for each case

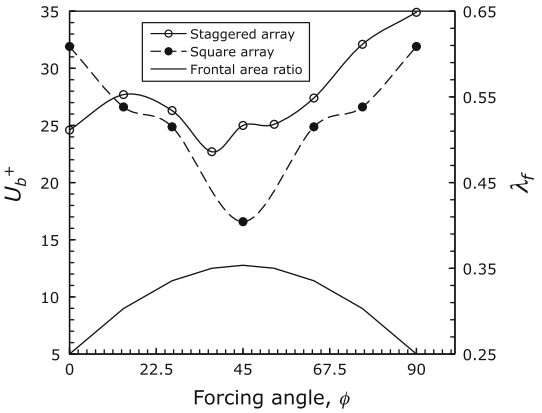

Fig. 9 Variation of the bulk velocity with forcing direction. Note that the lower solid line (without *symbols*) shows the variation of the frontal area ratio, λ_f

rate from $\phi = 0$ to 45°—practically 50%—is, however, rather surprising. But there is a large difference in the drag coefficient of an isolated cube mounted deep in a boundary layer for wind angles of 0° and 45°. From the measured surface pressure data on such a cube reported by, for example, Castro and Robins (1977), the ratio of the drag for $\phi = 45°$ to that for $\phi = 0°$ can be estimated to be roughly 2.7. The upstream velocity profile was identical in the two cases. For the present case, however, the arrays generate an effective mean velocity profile seen by each individual cube that varies with ϕ, as seen above. For the sake of argument, taking the velocity at $z = 1.25h$ as a suitable reference, the profile data in Fig. 8b imply that, if the same reference velocity were required at $\phi = 45°$ as at $\phi = 0°$, the forcing stress would have to be increased by a factor of about 3.0. This varies by less than 1% for reference velocity height choices in the range $1.15 < z/h < 1.45$ and is not very far from the above estimated drag ratio (2.7) for an isolated cube in the same flow.

In the case of the staggered array, the variations in U_b^+ are not of course symmetric about $\phi = 45°$ (see Fig. 9). With ϕ increasing from zero, a minimum is reached around $\phi = 38°$ but not before an intermediate maximum occurs. The latter is almost certainly a result of the fact that, at $\phi = 27°$, there happens to be a completely unobstructed 'street' through the array. This has a width of $0.45h$ and thus provides a narrow flow passage, allowing a greater flux than is possible at $\phi = 45°$. As ϕ increases beyond 45° U_b^+ rises almost monotonically, partly because, although there are no more wind directions that lead to *completely* unobstructed streets (until ϕ is exactly 90°), there are increasingly long street areas in the wind direction and also because the drag of individual cubes begins to fall again.

A further implication of the velocity data in Fig. 8 is that for the staggered array in the range $0° < \phi < 53°$ the mean flow direction in (most of) the lower half of the canopy is within 15° of the short-street direction (x_d in Fig. 3) quite independently of the forcing direction. This is not immediately obvious from Fig. 8a and might seem surprising; the implication is that at least in the spatially-averaged sense one could not deduce the forcing (and overall flow) direction simply by considering the flow direction near ground level. The reasons become clearer when considering the detailed 3D flow vector patterns (see later) but it should be noted that this result is quite different from the behaviour for the square array, emphasizing the crucial importance of the surface morphology in determining the canopy flow.

These various results all demonstrate that the overall influence on surface drag and thus bulk flow arises from a combination of the drag of individual obstacles and the degree of obstruction caused by the entire array. We can conclude also that the effects of orientation of the individual roughness obstacles are significantly more important than is the overall effect

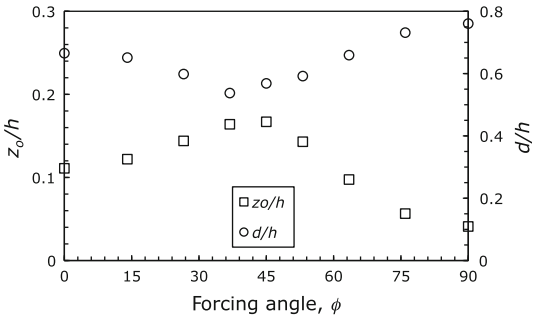

Fig. 10 Variations of roughness length and zero-plane displacement for the staggered array

of the changing blockage with orientation, expressed by λ_f (at least for cube arrays). All this is of course partly a result of the nature of the flow within the canopy region but before considering this (in the next section) it is worth mentioning the variations of the logarithmic law fitting parameters implied by the profiles in Fig. 8, i.e. the roughness length, z_o, and zero-plane displacement d.

Figure 10 shows the variation with ϕ of z_o/h and d/h for the staggered array. These were determined by fitting the spatially-averaged velocity profiles shown in Fig. 8a to the expected logarithmic law, $U^+ = \frac{1}{\kappa}\ln(z-d)/z_o$, as described by Coceal et al. (2006) with modifications similar to those proposed by Leonardi and Castro (2010). Specifically, this required firstly determining the zero-plane displacement by assuming (following Jackson 1981) that it is the height at which the drag force acts (in the flow direction), which was computed directly from the cube's surface pressure field (thus ignoring the small contributions from frictional forces). Secondly, the friction velocity was taken as $u_\tau\sqrt{1-d/H}$ and κ adjusted to yield the best fit. As Leonardi and Castro (2010) found, this yields the most satisfactory fit to the velocity data—significantly better than fixing κ at, say, 0.41 and adjusting d/h to yield a best fit—and it gives values of κ in the range 0.28–0.31. The details are not important here, but note that using the more common approach (i.e. fixing κ and adjusting d) yields values of z_o/h typically around a factor of two lower whilst giving exactly the same trend as is evident in Fig. 10. It is clear that the highest z_o/h, which occurs around $\phi = 45°$, is a factor of four higher than the lowest (at $\phi = 90°$) and, not surprisingly, follows roughly the same overall trend with ϕ as the inverse of U_b^+ (Fig. 9), i.e. larger roughness lengths correspond to larger drags and thus smaller bulk flow. Note also that the variation in d/h, whilst not insignificant, is very much smaller than that of z_o/h, lying in the range 0.54–0.76.

4.2.2 Canopy-Flow Details

Although the flow within the canopy is strongly inhomogeneous, it is of interest to consider first the spatially-averaged flow. Figure 11 shows how the flow direction varies with height, for a selection of the forcing directions. The ordinate axis, $\theta_u - \phi$, is the flow angle referred to coordinates aligned with the flow direction, i.e. the flow angle at the top of the domain, so that all the profiles tend to zero at $z = H$ (i.e. $\theta_u(H) - \phi = 0$, see Fig. 3). It is immediately clear that, although little flow turning occurs above the canopy, there are substantial directional variations within it. Furthermore, for a given forcing direction, $\phi = 27°$ for example, the flow direction within the square array (Fig. 11b) tends to align increasingly (with falling z) towards the direction of the unobstructed streets—but not perhaps the expected streets; one might have anticipated that the average flow would tend to align along the streets closest to the forcing direction—i.e. along $\theta = -27°$, whereas it actually tends to align towards the

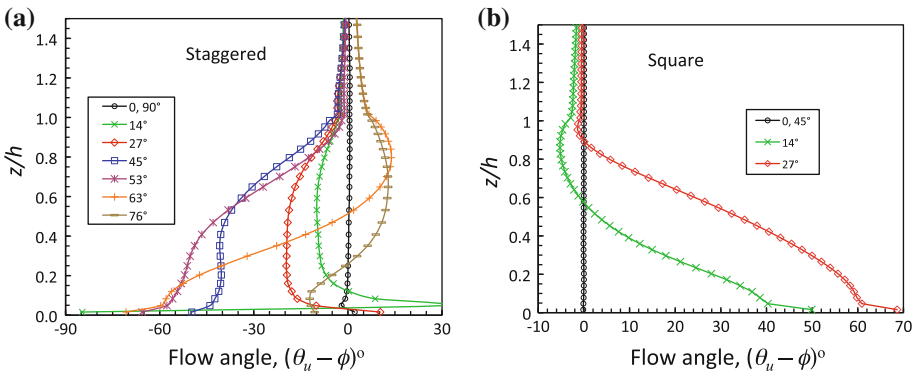

Fig. 11 Variations of flow angle within the canopy, with respect to the forcing direction, ϕ. The *legend* gives the values of ϕ

streets along $\theta = 90°$, so that $\theta_u(z) - \phi$ tends towards $90° - 27° = 63°$ in the lowest region of the canopy. (Recall the coordinate definitions in Fig. 3.) Similarly, for the staggered array (Fig. 11a) the flow tends to align along the $\theta = 0°$ direction, rather than along the wholly unobstructed direction $\theta = 90°$, so that $\theta_u - \phi = 0°$, even for forcing directions closer to $\theta = 90°$. See, for example, the data for $\phi = 63°$ in Fig. 11a, which become quite close to $\theta_u - \phi = -63°$ near $z/h = 0$. It is also interesting that, for the staggered array, a number of mid-range forcing directions lead to relatively small variations of average flow angle in the bottom half of the canopy, as the data for $\phi = 27°$, 45° and 53° in Fig. 11a show.

It is not immediately obvious why these average flow directions in the two arrays behave as they do, but consideration of the detailed, spatially variant flows at different heights within the canopy is instructive. First, Fig. 12 shows flow vectors for the staggered and square arrays for the forcing directions $\phi = 0°$ and 27°. At $\phi = 0°$ (Fig. 12a,b) the variations with height of these vector patterns are quite small, so only the $z/h = 0.5$ data are shown as typical. It is clear that, although there are evident recirculation regions behind the cubes in each array, the velocities within them are small; although local variations in wind angle in these regions can be large, symmetry ensures that the spatially-averaged wind angle at each height is zero, as Fig. 11b indicates. However, at non-zero forcing directions the structure of the local winds within the canopy is significantly different in the square array. Although for the staggered array there is again little variation with height, at least in the lower half of the canopy (only the $z/h = 0.5$ data are shown, see Fig. 12c), and the flow is not too dissimilar to that at $\phi = 0°$ (compare Fig. 12a and c), in the square array there are very large differences with height, as seen by comparing Fig. 12d ($z/h = 0.5$) with Fig. 13a,b ($z/h = 0.3$, 0.8, respectively) where it is evident that the flow is very different to that in the staggered array. Note in particular that at the lower heights, typified by Fig. 12d and Fig. 13a, the presence of a relatively large separation region on one side of the cubes is consistent with the flow being predominantly along the streets in the $\theta_u = 90°$ direction, rather than along the streets more closely aligned to ϕ. As z increases, this effect weakens significantly (compare Fig. 13a and b). Smaller non-zero forcing angles (i.e. $\phi = 14°$) yield similar behaviour. It is these various features that lead to the very different behaviour of the spatially-averaged flow angle profiles noted earlier (Fig. 11) for $\phi = 14°$ and 27°.

Other significant differences are apparent for higher forcing directions. Figures 14 and 15 show several vector patterns for $\phi = 45°$ and 63°. In the former case, the staggered and square array fields are very different (Fig. 14a,b). In the staggered array, the flow directly

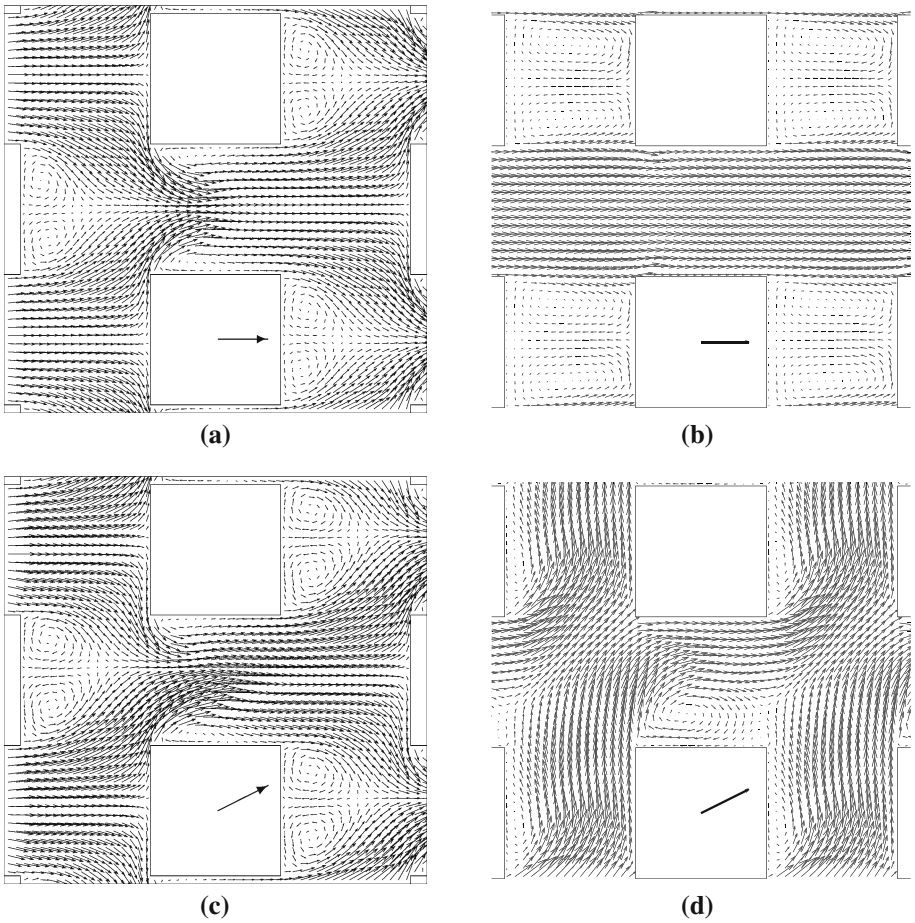

Fig. 12 Flow vectors at $z/h = 0.5$ within the canopy for staggered (**a**,**c**) and square (**b**,**d**) arrays at $\phi = 0°$ (**a**,**b**) and $\phi = 27°$ (**c**,**d**)

between the cubes $3h$ apart is characterized by small recirculation regions (almost symmetric) followed by strong flow largely in the $\phi - 45°$ direction, i.e. along the short streets. On the other hand, the square array case is typified by 'flow splitting' in the street intersection region, with flow between the cubes then largely following the local street direction. So, whilst in the latter case the average flow angle is around zero (see Fig. 11b), in the staggered array it is roughly in the $\phi - 45°$ direction (Fig. 11a). Variations in these patterns with height are small, except in the staggered case where above $z/h \approx 0.5$ the flow increasingly tends towards the forcing direction. For $\phi = 63°$ (Fig. 15) it is interesting that the flow field differences between $z/h = 0.3$ and 0.8 are sufficient to cause a change of sign in the average flow angle (θ_u°), as is clear in Fig. 11a.

5 Further Discussion and Conclusions

There are a number of significant conclusions to be drawn from the results. First, the pressure drag data of Fig. 6 show that the frictional effects can be significantly higher than they are for

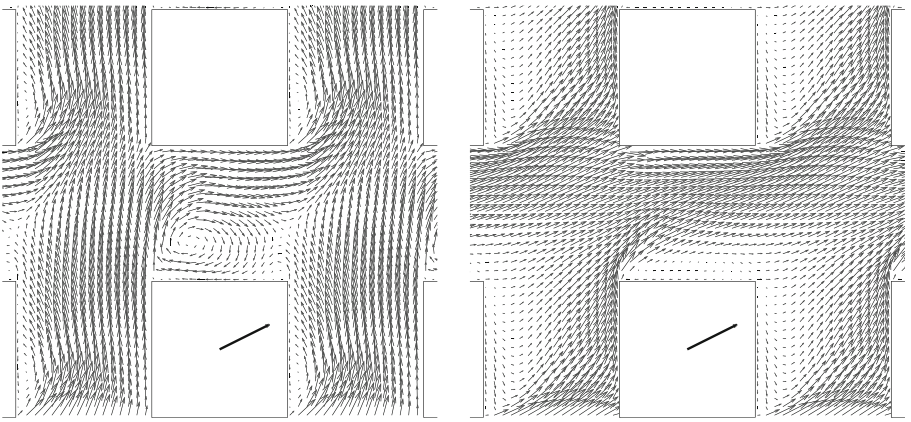

Fig. 13 Flow vectors within the canopy for the square array at $\phi = 27°$; $z/h =$: **a** 0.3; **b** 0.8

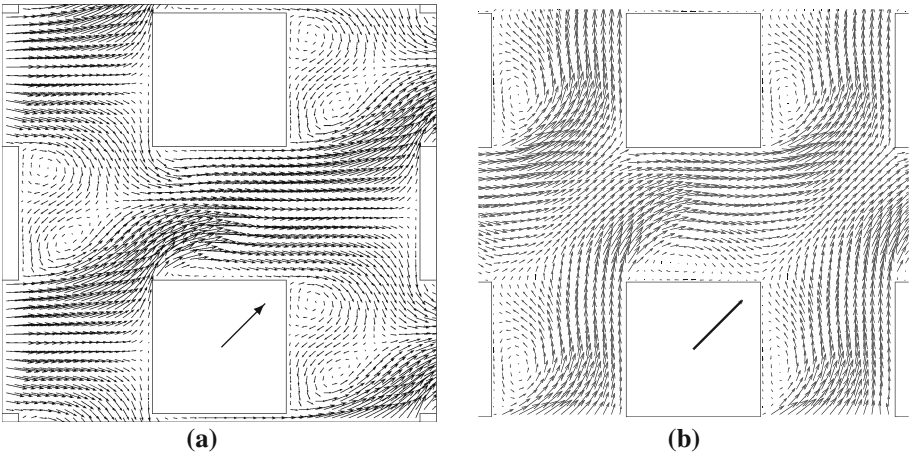

Fig. 14 Flow vectors within the canopy for staggered (**a**) and square (**b**) arrays at $\phi = 45°$ and $z/h = 0.5$

the staggered array in the fully blocked orientation ($\phi = 0°$). Indeed, they provide in excess of 30% of the total surface drag at $\phi = 90°$ for both array types (and likewise for the square array at the equivalent $\phi = 0°$ orientation). This result has been confirmed for the staggered array by high-resolution DNS (Leonardi, 2011, private communication, using the same code as employed by Leonardi and Castro (2010)). It raises the question of Reynolds number (Re) independence, for frictional drag components must be dependent on Re and will fall as it rises, as indeed the Leonardi and Castro (2010) work showed. The present computations were undertaken for $Re_\tau = u_\tau h/\nu = 500$, which would normally be considered sufficiently high for such surfaces to be essentially 'fully rough' (classically defined as rough enough to make frictional effects irrelevant). But it seems that for certain morphologies and wind directions, even these surfaces comprising only sharp-edged obstacles require significantly higher Re_τ before they become fully rough. Precisely how high will require further computations at much higher Reynolds numbers. An immediate implication, however, is that the

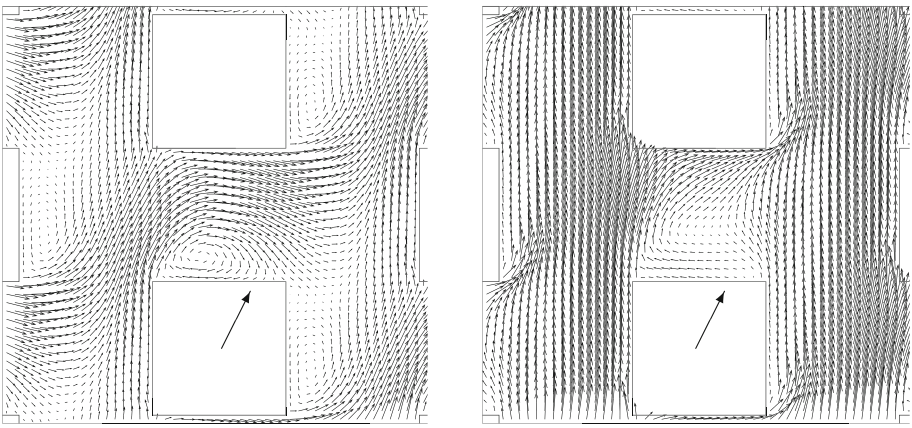

Fig. 15 Flow vectors within the canopy for staggered array at $\phi = 63°$ and $z/h =$: **a** 0.3; **b** 0.8

remaining conclusions should be viewed with the caveat that the present flows are not all, in fact, Reynolds number independent. Furthermore, the influence of the precise boundary conditions within the canopy used in LES approaches might have more importance than had been previously supposed (as, for example, by Xie and Castro, 2006), since these will determine the accuracy of the surface frictional forces. Note that there are not likely to be any genuine logarithmic law regions within the thin boundary layers on these surfaces.

Secondly, the data have demonstrated that in general the surfaces produce a non-zero lateral (lift) pressure force on the flow, as anticipated from the general considerations presented in Sect. 2. This seems not to have been recognized before. The computations suggest that this force is always small compared with the force in the wind direction (the drag). For the two surface morphologies considered, it never exceeds 7% of the latter. Because these are channel-flow computations with periodic boundary conditions, the pressure (lift and drag) forces, when referred to coordinates aligned with the forcing direction, yield a lateral force that is balanced by an equal and opposite frictional force, but in wind-tunnel experiments (or in the field) this balance is not a requirement. In either case, non-zero lateral force implies a small flow turning with height so that, in the present computations, there is a small difference between the forcing direction and the flow direction at the top of the domain (and much larger, but unrelated, flow turning can occur inside the canopy). No previous measurements or computations of the effects of wind direction (Kim and Baik 2004; Bezpalcova 2006; Hagishima et al. 2009) have mentioned lateral forces nor their consequences for flow turning, although Dejoan et al. (2010) did note some flow turning.

Thirdly, the evidence is clear that changing wind direction over a particular surface morphology can lead to very significant changes in the total drag imposed by the surface. The implications of the present computations are that changes in total drag may be as high as 300%, for wind directions that lead to sufficiently large changes in the drag coefficient of the individual obstacles. There are consequent changes in the parameters used to characterize the wind profile above the roughness via the usual logarithmic law. In particular, the roughness length z_o can change by a factor of four for 45° changes in wind direction. This has never been explicitly recognized in, for example, operational (weather forecasting) codes, which simply specify a single z_o deemed to be appropriate for the surface type. Uncertainties in

the changes in frictional forces due to Reynolds number differences between the present computations and those in the field are very unlikely to change this conclusion. However, it is worth noting that the only published direct drag measurements for a surface at (just two) orientations to the wind (Hagishima et al. 2009, who used a floating balance to measure total drag) suggest a drag change of about a factor of two between $\phi = 0°$ and 45° for a square array of cubes, about 70% of that implied by the present data. Some of this difference may be due to the different (effective) values of H/h in the former case; the Hagishima et al. (2009) experiments used a boundary layer whose height, δ was presumably set by the upstream spires and although they did not give a value for δ/h it was probably significantly higher than the $H/h = 4$ used in the present computations. It may be that the more restricted outer region of the surface 'boundary layer' in our channel flow cases amplifies somewhat the changes in drag with wind direction. This point requires further clarification, but it should be mentioned that wind-tunnel experiments undertaken simultaneously with the present computations, having typically $\delta/h = 8$, yielded very similar drag change values for the staggered array case as found in the channel computations presented here (Claus 2011).

Fourthly, the flows within the canopy region are clearly very dependent on wind direction aloft. However, there are situations in which large changes in the latter only marginally change the spatially-averaged flow direction in the bottom half of the canopy (as has been noted before by e.g., Belcher 2005; Wood et al. 2009). Overall, the canopy flow tends to be directed along the streets, although when these are of very limited extent there are often very significant changes in local wind direction with height. The finding that near the bottom of the canopy average wind directions can be largely independent of the wind direction aloft is very similar to the recent result of Xie (2011) in the context of the DAPPLE field site in central London (Dobre et al. 2005). He found that wind directions of both 90° (along the Marylebone Road) and 51° (quite close to the prevailing south-west wind direction) led to very similar near-surface average wind directions. This was partly a result of slight stagger in the building arrangements on the north side of Marylebone Road and, as in some of the present results, there was a large variation in average wind direction with height within the canopy and these computational results were similarly apparent in the wind-tunnel model simulations of flow and dispersion at the DAPPLE site.

The very inhomogeneous canopy flows, strongly influenced by canopy morphology, naturally have significant effects on the dispersion of pollutants emitted within the canopy. This has already been shown by numerous authors, not least by Bezpalcova (2006) and Yee and Biltoft (2004) who also, particularly pertinent in the present context, identified some of the changes in concentration levels caused by wind direction changes for the case of a (wind-tunnel) model of the MUST field experiments described by Biltoft (2001). This used a significantly less dense array of (non-cubic) container-like obstacles, compared with the present cases, so that flow channelling along streets was more ubiquitous. Such channelling and the effect of spiral street vortices caused by flow directions not aligned with the streets have also been demonstrated in the work surrounding the DAPPLE project (Dobre et al. 2005). In particular, Xie (2011) has shown computationally how a change in wind direction to 90° from 51°, with respect to the major street orientation, affects not only the nature of the canopy flow, as noted above, but also the maximum street-level concentration levels arising from a point source within the canopy. Mean maximum concentration levels differed typically by a factor of about two for the two wind directions. Consideration of these recent (but somewhat limited) studies including wind direction issues along with the results of the present computations suggests strongly that quantitative flow details and consequent mean and fluctuating concentration levels are always going to be dependent not only on specific

canopy morphology but also on prevailing wind direction; the likelihood of being able to predict them without specific simulations that account for both is thus remote.

We remark finally that one might ask, for example, how the 'portal vortices' identified by Hagishima et al. (2009) might be affected by wind direction, or how the strong link between the outer flow organized longitudinal turbulent structures and the near-ground canopy flow identified by Inagaki et al. (2012) might be affected by wind flow directions that do not yield along-wind streets in the surface morphology. Whilst such questions are not without fundamental interest, from a practical perspective the crucial global issues concern, rather, how wind direction affects the variability in total (mean) surface drag, consequent changes to inertial layer parameters, and overall canopy flows. It is these that have been addressed in the present work, with the major conclusions summarized above.

Acknowledgments This project is funded by the Natural Environment Research Council (NERC). We are grateful for a NERC studentship supporting the first author, support for for OC from NERC through their National Centre for Atmospheric Science (grant no. R8/H12/83), helpful interactions with staff at CD-adapco and informative discussions with our (Southampton) colleagues, Drs. Z-T Xie and B. Boppana.

References

Barlow JF, Belcher SE (2002) A wind tunnel model for quantifying fluxes in the urban boundary layer. Boundary-Layer Meteorol 104:131–150

Belcher S (2005) Mixing and transport in urban areas. Philos Trans Roy Soc A363:2947–2968

Bezpalcova K (2006) Physical modelling of flow and diffusion in urban canopy. PhD thesis, Charles University, Prague

Biltoft C (2001) Customer report for mock urban setting test. Tech. Rep. WDTC-FR-01-121, U.S. Army Dugway Proving Ground, Dugway, UT

Branford S, Coceal O, Thomas TG, Belcher SE (2011) Dispersion of a point-source release of a passive scalar through an urban-like array for different wind directions. Boundary-Layer Meteorol 139:367–394

Castro IP, Robins AG (1977) The flow around a surface-mounted cube in uniform and turbulent streams. J Fluid Mech 79:307–335

Cheng H, Castro IP (2002) Near-wall flow over urban-like roughness. Boundary-Layer Meteorol 104:229–259

Claus J (2011) Wind direction effects on urban flows. PhD thesis, Engineering Sciences, University of Southampton

Coceal O, Belcher SE (2004) A canopy model of mean winds through urban areas. Q J Roy Meteorol Soc 139:1349–1372

Coceal O, Thomas TG, Castro IP, Belcher SE (2006) Mean flow and turbulence statistics over groups of urban-like cubical obstacles. Boundary-Layer Meteorol 121:491–519

Davidson MJ, Mylne KR, Jones CD, Phillips JC, Perkins RJ, Fung JCH, Hunt JCR (1995) Plume dispersion through large groups of obstacles—a field investigation. Atmos Environ 29:3245–3256

Dejoan A, Santiago J, Martilli A, Martin F, Pinelli A (2010) Comparison between large-eddy simulation and reynolds-averaged navier stokes computations for the must field experiment part ii: effects of incident wind angle deviation on the mean flow and plume dispersion. Boundary-Layer Meteorol 135:133–150

Dobre A, Arnold SJ, Smalley RJ, Boddy JWD, Barlow JF, Tomlin AS, Belcher SE (2005) Flow field measurements in the proximity of an urban intersection in London, UK. Atmos Environ 39:4647–4657

Hagishima A, Tanimoto J, Nagayama K, Meno S (2009) Aerodynamic parameters of regular arrays of rectangular blocks with various geometries. Boundary-Layer Meteorol 132:227–315

Hanna SR, Thranian S, Carissimo B, MacDonald RW, Lohner R (2002) Comparisons of model simulations with observations of mean flow and turbulence within simple obstacle arrays. Atmos Environ 36: 5067–5079

Hanna SR, Brown MJ, Camelli FE, Chan ST, Coirier WJ, Hansen OR, Huber AH, Kim S, Reynolds RM (2006) Detailed simulations of atmospheric flow and dispersion in downtown Manhattan. Bull Am Meteorol Soc 87:1713–1726

Inagaki A, Castillo M, Yamashita Y, Kanda M, Takimoto H (2012) Large-eddy simulations study of coherent flow structures within a cubical canopy. Boundary-Layer Meteorol. doi:10.1007/s10546-011-9671-8

Jackson PS (1981) On the displacement height in the logarithmic velocity profile. J Fluid Mech 111:15–25

Kanda M, Kanega M, Kawai T, Moriwaki R (2007) Roughness lengths for momentum and heat derived from outdoor urban scale models. J Appl Meteorol Climatol 46:1067–1079

Kastner-Kline P, Rotach MW (2005) Mean flow and turbulence characteristics in an urban roughness sublayer. Boundary-Layer Meteorol 111:55–84

Kim J, Baik J (2004) A numerical study of the effects of ambient wind direction on flow and dispersion in urban street canyons using the RNG k–epsilon model. Atmos Environ 38:3039–3048

Leonardi S, Castro IP (2010) Channel flow over large cube roughness: a DNS study. J Fluid Mech 651:519–539

Perry SG, Heist DK, Thompson RS, Snyder WH, Lawson RE (2004) Wind tunnel simulation of flow and pollutant dispersal around the World Trade Centre site. Environ Manager February:31–34

Rotach MW (1993) Turbulence close to a rough urban surface, Part I: Reynolds stress. Boundary-Layer Meteorol 65:1–28

Roth M (2000) Review of atmospheric turbulence over cities. Q J Roy Meteorol Soc 126:941–990

Takimoto H, Sato A, Barlow JF, Moriwaki R, Inagaki A, Onomura S, Kanda M (2011) Particle image velocimetry measurements of turbulent flow within outdoor and indoor urban scale models and flushing motions in urban canopy layers. Boundary-Layer Meteorol 140:295–314

Wood C, Arnold S, Balogen A, Barlow J, Belcher S, Britter R, Cheng H, Dobre A, Lingard J, Martin D, Neophytou M, Petersson F, Robins A, Shallcross D, Smalley R, Tate J, Tomlin A, White I (2009) Dispersion experiments in central London. Bull Am Meteorol Soc 90:956–965

Xie ZT (2011) Modelling street-scale flow and dispersion in realistic winds—towards coupling with mesoscale meteorological models. Boundary-Layer Meteorol 141:53–75

Xie ZT, Castro IP (2006) LES and RANS for turbulent flow over arrays of wall-mounted obstacles. Flow Turbul Combust 76:291–392

Xie ZT, Coceal O, Castro IP (2008) Large eddy simulation of flows over random urban-like obstacles. Boundary-Layer Meteorol 129:1–23

Yamartino RJ, Wiegand G (1986) Development and evaluation of simple models for the flow, turbulence and pollutant fields within an urban street canyon. Atmos Environ 20:2137–2156

Yao YF, Thomas TG, Sandham ND, Williams JJR (2001) Direct numerical simulation of turbulent flow over a rectangular trailing edge. Theor Comput Fluid Dyn 14:337–358

Yee E, Biltoft C (2004) Concentration fluctuation measurements in a plume dispersing through a regular array of obstacles. Boundary-Layer Meteorol 111:363–415

Yoshizawa A (1986) Statistical theory for compressible turbulent shear flows, with the application to subgrid scale modelling. Phys Fluids 29:2152–2164